Sustainable Energy & Fuels

Carrier-gas Assisted Vapor Deposition for Highly Tunable Morphology of Halide Perovskite Thin Films

Journal:	*Sustainable Energy & Fuels*
Manuscript ID	SE-ART-03-2019-000200.R1
Article Type:	Paper
Date Submitted by the Author:	10-Jul-2019
Complete List of Authors:	Clark, Catherine; University of Minnesota Twin Cities, Chemical Engineering and Materials Science Voigt, Bryan; University of Minnesota Twin Cities, Chemical Engineering and Materials Science Aydil, Eray; New York University Tandon School of Engineering, Chemical and Biomolecular Engineering Holmes, Russell; University of Minnesota Twin Cities, Chemical Engineering and Materials Science

Sustainable Energy and Fuels

Carrier-gas Assisted Vapor Deposition for Highly Tunable Morphology of Halide Perovskite Thin Films

Catherine P. Clark,[a] Bryan Voigt,[a] Eray S. Aydil[b] and Russell J. Holmes[a]

Received 00th January 20xx,
Accepted 00th January 20xx

DOI: 10.1039/x0xx00000x

www.rsc.org/

We demonstrate carrier-gas assisted vapor deposition (CGAVD) as a promising synthesis technique for high-quality metal halide perovskite thin films. Wide tunability of film microstructure and morphology are accesible with CGAVD *via* the combination of several independently controllable experimental variables. Here, we examine in detail the material transport mechanisms in CGAVD and develop analytical expressions for deposition rates for the halide perovskite precursors MABr, MAI, $SnBr_2$, and SnI_2 as a function of experimentally tunable temperatures, pressures, and flow rates. The method is then applied to systematically control the growth of $MASnBr_3$ thin films via co-deposition across a range of stoichiometries and morphologies. In varying source material temperature, carrier gas flow rate, dilution gas flow rate, substrate temperature, and chamber pressure, corresponding changes are realized in the degree of crystallinity, grain orientation, and average grain size (from ~ 0.001 to $> 0.7\ \mu m^2$). Thin films of $MASnI_3$ and $MASnBr_3$ deposited using CGAVD show resistivities of 3 Ω cm and 7x10^4 Ω cm, respecitvely, broadly consistent with previous reports.

Introduction

Metal halide perovskites have gained significant attention as active materials for optoelectronic devices, due to their tunable electronic and optical properties and their compatibility with high-throughput processing on flexible substrates.[1–8] This interest has been amplified by the impressive performance of metal halide optoelectronics, with solar cell power conversion efficiencies exceeding 23%[9] and light-emitting diodes reaching external quantum efficiencies of >20%.[10]

It is widely acknowledged that film quality and morphology strongly impact device performance, as film microstructure can influence charge recombination and collection, shunting pathways, and ion migration kinetics.[1,11–19] In turn, microstructure is dictated by the film processing technique and specific crystallization conditions.[20] There is still much to understand regarding the interplay between synthesis conditions, film microstructure, and the resulting optoelectronic properties. The impact of grain boundaries on non-radiative recombination rates, for instance, is still an area of debate.[21–24]

Consequently, thin film deposition techniques that yield stoichiometrically precise, defect-free perovskite films with tunable morphology are becoming increasingly essential for device applications. Ideally, these techniques should be efficient in their use of materials, robust with respect to reproducibility, and scalable for high-throughput production.

These requirements have motivated a growing interest in vapor-based deposition techniques. The nascent body of work on vapor-deposited metal halide perovskites has already demonstrated deposition on large-area flexible substrates and fine control over film composition and morphology.[25,26,35–44,27,45–54,28,55–64,29,65,30–34] Moreover, vapor deposition can enable facile growth of multi-layer stacks, such as an interlayer-free 2-terminal perovskite-Si tandem cell,[66] thus providing a practical route to tandem and multi-layer perovskite solar cells.[67,68]

The most commonly employed vapor deposition methods utilize high-vacuum (~10^{-6} Torr) thermal evaporation (VTE), either by co-evaporation or sequential evaporation of the precursor materials.[25,26,42–47,27–32,40,41] An alternative but understudied approach is carrier-gas assisted vapor deposition (CGAVD), where an inert carrier gas such as N_2 or Ar is used to transport source material vapors to the substrate at pressures >0.1 Torr. CGAVD provides a large parameter space to tune film composition and microstructure *via* six independently controllable pressures, temperatures, and flow rates. Indeed, CGAVD has been previously explored in the context of organic semiconductors, demonstrating exquisite control of composition and morphology, and enabling the growth of planar and bulk heterojunction devices.[69–74]

For metal halide perovskites, however, CGAVD has been only sporadically used. Jiang *et al.* and Leyden *et al.* have synthesized $Cs_xFA_{1-x}PbI_3$, $MAPbBr_3$, and $MAPbI_xCl_{3-x}$[35,38,59,75] using a “hybrid”

[a] Department of Chemical Engineering and Materials Science University of Minnesota, Minneapolis MN 55455
[b] Department of Chemical and Biomolecular Engineering, Tandon School of Engineering, New York University, Brooklyn, NY, 11201
Electronic Supplementary Information (ESI) available: [details of any supplementary information available should be included here]. See DOI: 10.1039/x0xx00000x

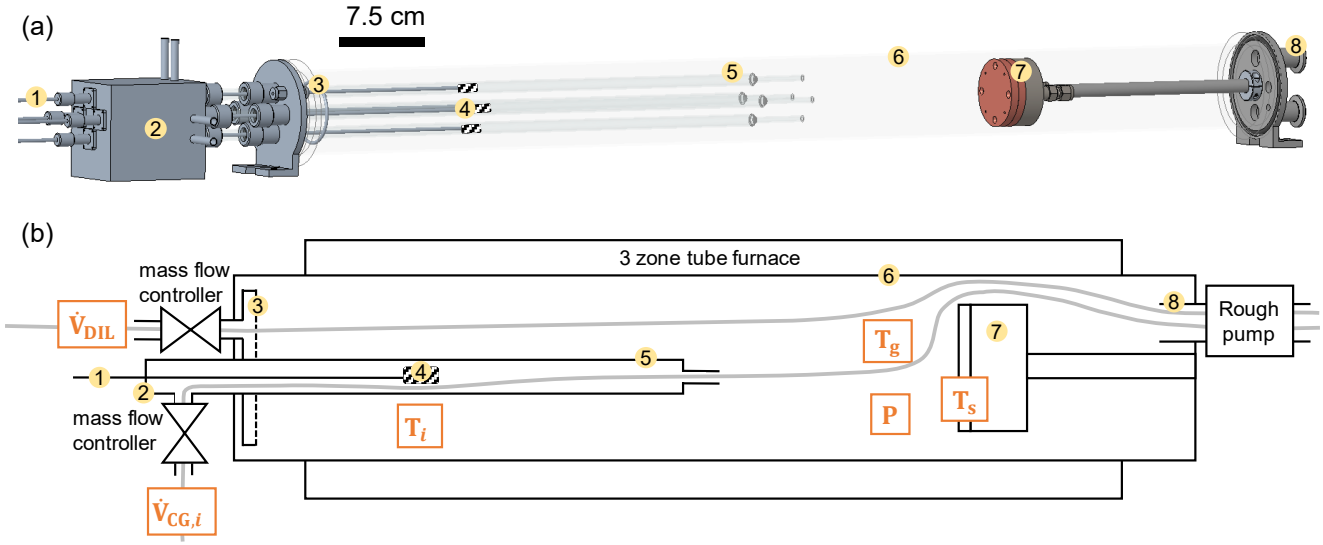

Fig. 1 Schematics describing the CGAVD system used in this work. Part numbers are defined as follows: (1) linear actuator with embedded thermocouple; (2) N_2 carrier gas manifold; (3) showerhead for dilution gas delivery; (4) source material attached to linear actuator; (5) source material tube; (6) 3" diameter quartz chamber; (7) water-cooled substrate holder; (8) ports for rough pump. (a) CAD model (to scale) of 4-source CGAVD system. (b) Schematic highlighting the six independent experimental parameters in CGAVD (orange boxes): the carrier gas flow rate $\dot{V}_{CG,i}$; the dilution gas flow rate $\dot{V}_{DIL}$; the source material temperature T_i; the gas temperature T_g; the substrate temperature T_s; and the deposition pressure P.

approach, where the metal halide (*e.g.* PbI_2) film is first deposited using a solution or high-vacuum process, and then CGAVD is used to expose that film to the organic halide (*e.g.* MAI).[35,38,59,75,76] Power conversion efficiencies exceeding 15% have been achieved with perovskite films deposited using these two-step hybrid processes.[36,76,77] We are aware of only two reports where the full perovskite film is deposited using CGAVD. Wang *et al.* use CGAVD to achieve epitaxial growth of single-crystal $CsPbBr_3$ and $CsSnBr_3$ on NaCl substrates.[78] Tavakoli *et al.* form ~1 µm grained, pinhole free $MAPbI_{3-x}Cl_x$ films *via* CGAVD for incorporation into 11.1% efficient photovoltaic cells.[34] However, no comprehensive exploration of the morphologies accessible using CGAVD has been reported, and consequently there is substantial room for further exploration and development of this promising technique.

In order to harness the full potential of CGAVD, a detailed understanding is needed of how changes in system pressures, temperatures, and flow rates impact film microstructure. Here, the impact of each parameter on source material transport and substrate deposition rate is examined. By developing an analytical model for deposition rate, operating regimes are identified that lead to robust and repeatable film growth. Further systematic tuning of CGAVD experimental parameters is applied to engineer the microstructure and stoichiometry of $MASnBr_xI_{3-x}$ thin films, including the degree of crystallinity, grain orientation, and grain size.

Experimental Methods

$MASnBr_xI_{3-x}$ thin films were deposited using the CGAVD system shown in Fig. 1. This system consists of a 3" diameter quartz tube inside a three-zone cylindrical furnace. The axial temperature profile within the tube is controlled by the furnace temperature set points. Four 0.5" diameter quartz tubes are positioned eccentrically inside the larger 3" tube. Within each 0.5" tube, source material powder (*e.g.*, MABr, MAI, $SnBr_2$, or SnI_2) is packed in a porous frit and attached to a linear feedthrough with embedded thermocouples for real-time temperature monitoring. These linear feedthroughs are used to translate the sources axially to vary source material temperature.

Nitrogen, the carrier gas, flows through each source tube and over the source material, carrying sublimed vapor towards a cooled substrate. The tubes-within-tubes arrangement with independent carrier gas flows for each source minimizes back flow and source material contamination. Additional N_2 is fed into the annular region around the source material tubes. This flow dilutes the vapors emerging from the source tubes, providing additional control over the species fluxes independent from the source material evaporation rate and chamber pressure. After exiting the source tube, the vapors impinge, condense, and/or react on the cooled substrate to form films.

Six independent experimental parameters can be varied (Fig. 1b) to alter the deposition of a source material *i*: the carrier gas flow rate $\dot{V}_{CG,i}$; the chamber dilution gas flow rate $\dot{V}_{DIL}$; the source material temperature, T_i; the chamber gas temperature T_g; the substrate temperature, T_s; and the total chamber

pressure, P. All gas flow rates are set and maintained constant during deposition by mass flow controllers. The substrate temperature, T_s, is adjusted by changing cooling water temperature. The total pressure, P, is controlled by a combination of dilution gas and a valve before the pump. Typical values of the deposition parameters for synthesizing the $MASnBr_xI_{3-x}$ thin films reported herein are listed in Table 1. Additional experimental details are provided in the Supporting Information.

Given the vast parameter space of CGAVD, it is imperative that a systematic and informed approach is adopted when developing this technique for metal halide perovskite depositions. For instance, a combination of low T_i and high $\dot{V}_{CG,i}$ during deposition can cause deposition rates to depend on the source material surface area (Fig. S1), which is difficult to control and thus can introduce significant run-to-run variation.

Following Shtein *et al.*,[71] an analytical model of mass transport in CGAVD was developed and used to calculate precursor species fluxes arriving at the substrate. A detailed treatment for a wide range of deposition conditions can be found in the Supporting Information. For the deposition conditions used herein, the flux of a material *i* at the surface of the substrate (r_i) can be expressed as

$$r_i = C_{1,i} \cdot \frac{P_0 T_g}{R T_0} \cdot \frac{\dot{V}_{CG,i}}{P \cdot T_i} \cdot e^{\frac{-\Delta H_i^S}{R}\left(\frac{1}{T_i} - \frac{1}{C_{2,i}}\right)}, \quad \text{Eqn. 1}$$

where $C_{1,i}$ and $C_{2,i}$ are material-specific constants (see Table S1), ΔH_i^S is the sublimation enthalpy, R is the universal gas constant, $P_0 = 760$ Torr, and $T_0 = 25$ °C. Eqn. 1 elucidates the functional impact of different experimentally adjustable variables on the deposition rate. As r_i has an exponential dependence on T_i, source material temperature can be used to make large changes in deposition rate. The dependence of deposition rate on $\dot{V}_{CG,i}$, T_g, and P however, is linear, and these parameters can be used to easily make smaller, incremental adjustments in r_i.

To validate and calibrate the model in Eqn. 1, neat films of MABr, MAI, $SnBr_2$, and SnI_2 were deposited at a variety of temperatures, pressures, and flow rates, while keeping the substrate temperature constant ($T_s = 15$ °C). These data were used to extract the enthalpy of sublimation, ΔH_i^S, for each material (Table 2) which agree well with available reported values. See Fig. S2 for the experimental data and fits of Eqn. 1.

i	$\dot{V}_{CG,i}$ (sccm)	T_i (°C)	$\dot{V}_{DIL}$ (sccm)	T_g (°C)	T_s (°C)	P (Torr)
MABr	2 – 5	135 – 150	20 – 190	300	10 – 70	0.3 – 10
MAI	2 – 5	140 – 160				
$SnBr_2$	3 – 8	220 – 250				
SnI_2	8 – 10	240 – 270				

Table 1 Typical values for the experimental variables used to deposit $MASnBr_xI_{3-x}$ thin films using MABr, MAI, $SnBr_2$, and SnI_2 precursors.

i	ΔH_i^S **Fit** (kJ/mol)	ΔH_i^S **Lit** (kJ/mol)
MABr	83 [79, 85]	78 - 105 †
MAI	104 [91, 115]	105 ‡
$SnBr_2$	140 [126, 155]	135 †
SnI_2	180 [175, 186]	140 - 172 †⊥

Table 2 Enthalpies of sublimation for MABr, MAI, $SnBr_2$, and SnI_2 extracted from fitting experimentally measured deposition rates to Eqn. 1. Numbers in square brackets correspond to the 95% confidence intervals for these fits. Fig. S2 shows plotted fit data and fits vs. $\dot{V}_{CG,i}$ and T_i. No value for ΔH^S_{MABr} could be found in the literature; this range corresponds to the sublimation enthalpies for MACl and MAI,[88] which bound the value for MABr.‡[88]† [89]⊥[90]

With the extracted values for $C_{1,i}$, $C_{2,i}$ and ΔH_i^S, Eqn. 1 can be used to select processing conditions to deposit $MASnBr_xI_{3-x}$ films at desired deposition rates and compositions (*e.g.,* x=2). For co-depositions involving two materials (denoted A and B), the ratio r_A/r_B represents the ratio of precursor species available to react and form the perovskite at the substrate/film surface

$$\frac{r_A}{r_B} = \frac{C_{1,A}}{C_{1,B}} \cdot \frac{T_B}{T_A} \frac{\dot{V}_{CG,A}}{\dot{V}_{CG,B}} \cdot e^{\left[\frac{-\Delta H_{V,A}}{R}\left(\frac{1}{T_A} - \frac{1}{C_{2,A}}\right) - \frac{-\Delta H_{V,B}}{R}\left(\frac{1}{T_B} - \frac{1}{C_{2,B}}\right)\right]}. \quad \text{Eqn. 2}$$

Eqn. 2 implies that changes in film stoichiometry during co-deposition of components A and B can be realized through changes in $\dot{V}_{CG,A}$, $\dot{V}_{CG,B}$, T_A and/or T_B. Here, we define the normalized precursor excess $r_{A,B}$

$$r_{A,B} = (r_A - r_B)/\min(r_A, r_B), \quad \text{Eqn. 3}$$

where $r_{A,B} = 0$ indicates equal molar fluxes of species A and B, a negative value indicates excess metal halide (*e.g.,* $SnBr_2$) and a positive value indicates excess organic halide (*e.g.,* MABr).

Results and Discussion

Phase-Pure, Uniform $MASnBr_xI_{3-x}$ on a Variety of Substrates

Phase pure $MASnBr_3$ and $MASnI_3$ thin films were deposited *via* one-step co-deposition by manipulating $\dot{V}_{CG,i}$ and T_i according to Eqn. 2 such that $r_{MABr}/r_{SnBr2} \sim 1$ and $r_{MAI}/r_{SnI2} \sim 1$, respectively. Moreover, $MASnBr_xI_{3-x}$ ($0 < x < 3$) films were fabricated by depositing $MASnI_3$ on top of $MASnBr_3$ and using the relative thickness of each layer to achieve the desired stoichiometric ratio x. Deposition parameters for these films are listed in Table S2. Fig. 2 shows X-ray diffraction (XRD), optical absorption, and photoluminescence (PL) from films with x=0,

1.5, 2 and 3. These data are consistent with previous reports on $MASnBr_xI_{3-x}$ synthesized using other techniques.[52,79,80] XRD peaks shift monotonically to larger 2θ values with increasing Br content, from 16.5° (x=0) to 17.5° (x=3), implying a smooth phase-transition from tetragonal $MASnI_3$ to pseudocubic $MASnBr_3$ as described elsewhere.[80] Strong texturing along (001) is evident for x=0, 1.5, and 2. While texturing can be substantially tuned independent of stoichiometry using CGAVD, strong texturing is observed more readily for $MASnI_3$ films than $MASnBr_3$ films.

The measured optical absorption spectra (Fig. 2b) show absorption onsets decreasing from a wavelength of 880 nm for x=0 to 575 nm for x=3. Photoluminescence is observed at a wavelength of 730 nm for x=1.5 and 960 nm for x=0, with no significant PL from films with x≥2. This is consistent with

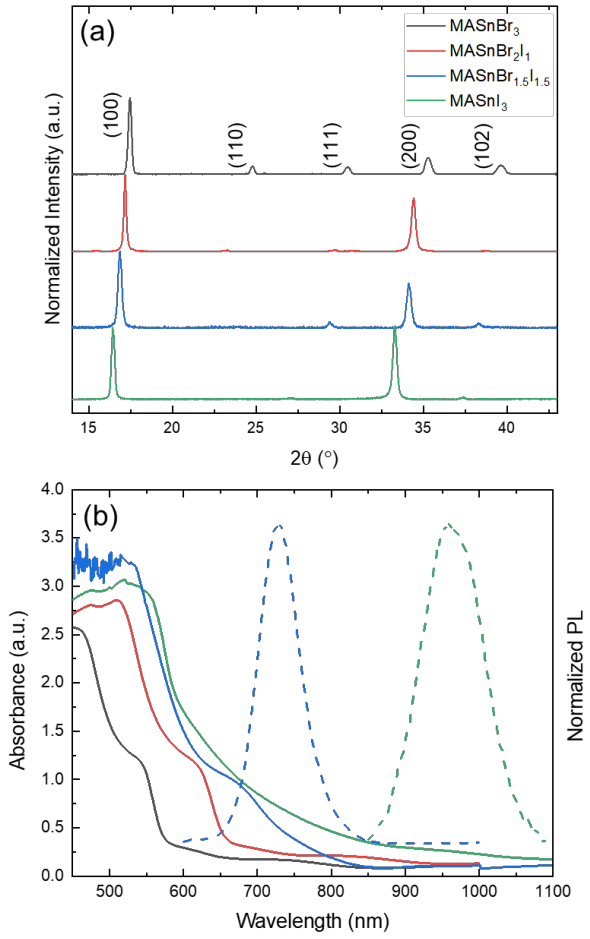

Fig. 2 (a) X-ray diffraction patterns of $MASnBr_3$, $MASnI_3$, and $MASnBr_xI_{3-x}$ films deposited on quartz using CGAVD. $MASnI_3$ and $MASnBr_xI_{3-x}$ films are highly oriented along [001], with small (111) and (102) peaks visible for $MASnBr_2I_1$. (b) Corresponding absorbance (solid lines) and photoluminescence (dashed lines) spectra. No significant photoluminescence is observed for x>1.5, which is consistent with previous reports. Film thicknesses are 450 nm, 310 nm, 130 nm, and 410 nm for x = 3, 2, 1.5, and 0, respectively. See Table S2 for deposition parameters for these films.

previous reports, where the PL efficiency was negligible (<0.1%) and no electroluminescence was observed from $MASnBr_xI_{3-x}$ films with x>1.5.[80]

Interestingly, the sequentially deposited $MASnBr_3$ and $MASnI_3$ films mix spontaneously even at substrate temperatures as low as 15 °C. To our knowledge, this is the first synthesis of $MASnBr_xI_{3-x}$ by sequential deposition of single-halide perovskite films. This rapid and spontaneous mixing implies high I^- and Br^- diffusion rates within the perovskite crystal structure. Based on this observation, $MASnBr_xI_{3-x}$ appears to be energetically favourable and stable at room temperature.

CGAVD deposited $MASnBr_xI_{3-x}$ films are uniform over large areas. $MASnBr_3$ grown on a silicon substrate, for example, has less than 10% thickness variation over 4 cm^2, the largest area that can be accommodated in the current CGAVD system. Due to the collimated flow reaching the substrate, uniformity over larger areas should be attainable with larger CGAVD systems or by rotating the substrate.

In addition to uniformity over large areas, CGAVD enables the formation of morphologically similar films on a variety of different substrates and on materials used as electron- and hole-transport layers. Fig. S3 shows the morphology of $MASnI_3$ and $MASnBr_3$ films grown on various substrates including PEDOT:PSS, c-TiO_2, Si, quartz, and indium-tin-oxide (ITO)-coated glass. The ability to deposit films with similar morphology on different surfaces provides an opportunity to conduct meaningful studies of the roles of electron- and hole-transport layers on films with comparable morphology.

Stoichiometric and Morphological Control *via* $\dot{V}_{CG,i}$ and T_i

Following Eqn. 2, $\dot{V}_{CG,i}$ and T_i (i = MABr, $SnBr_2$) were tuned to access a range of relative precursor fluxes and resulting film stoichiometries. Fig. S4a-f shows SEM images of films deposited on quartz with $-1 < r_{MABr,SnBr_2} < 1$. Deposition conditions for these films are shown in Table S3, and XRD patterns are shown in Fig. S5. Fig. S4g shows average grain size as a function of film stoichiometry, where the films' phase-purity is calculated using the diffraction peak intensity. The XRD peak intensity ratios I_{MABr}/I_{MASnBr_3} and I_{SnBr_2}/I_{MASnBr_3} are calculated by dividing the largest excess precursor (*i.e.,* MABr or $SnBr_2$) XRD peak intensity with that of the $MASnBr_3$ (100) peak (at 2θ=17.5°). Films are deemed "stoichiometric" if there are no observable diffractions from MABr or $SnBr_2$. Average grain area is calculated by applying the Weka Trainable Segmentation tool in ImageJ to several SEM images taken from different locations on each substrate. Representative images and resulting grain boundaries are shown in Fig. S6.

Films with excess MABr or excess $SnBr_2$ are observed to have non-ideal microstructures. MABr-rich films have large grains (up to 10 μm^2 for Fig. S4a) but exhibit incomplete coverage and domains that appear to be perovskite grains surrounded by excess MABr. $SnBr_2$-rich films exhibit small-grained structures

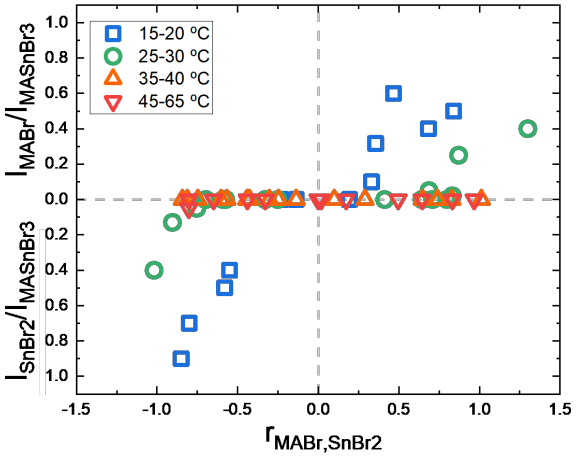

Fig. 3 Impact of T_s on stoichiometrically "self-correcting" window for $MASnBr_3$ films on quartz. For low T_s of 15 – 20 °C, an imbalance of precursor fluxes results in non-stoichiometric films for $|r_{MABr,SnBr2}| > 0.3$. This window increases for warmer T_s of 25 – 30 °C where stoichiometric films are formed for $|r_{MABr,SnBr2}| < 0.7$. For T_s > 35 °C, this range extends further, such that a flux imbalance of 100% for either $SnBr_2$ or MABr still results in a stoichiometric film.

that have significant pinholes, cracks, and ill-defined grain boundaries (Fig. S4 e,f). In contrast, stoichiometric films exhibit large (0.2 μm²), well-defined grains and dense substrate coverage (Fig. S4 d).

Interestingly, during these growths it was observed that on some occasions, non-zero $r_{MABr,SnBr2}$ resulted in stochiometric films; *i.e.* even without perfectly balanced precursor fluxes, no excess precursor peaks were observed in the XRD patterns. To investigate this further, $MASnBr_3$ depositions were carried out at a variety of $\dot{V}_{CG,i}$ and T_i (i = MABr, $SnBr_2$), and a range of substrate temperatures T_s. Fig. 3 shows that the range of $r_{MABr,SnBr2}$ which results in stoichiometric films depends strongly on T_s. For low T_s of 15 – 20 °C, an imbalance of precursor fluxes results in non-stoichiometric films for $-0.3 < r_{MABr,SnBr2} < 0.3$. This window increases for warmer T_s of 25 – 30 °C, where stoichiometric films are formed up to flux imbalances of $-0.7 < r_{MABr,SnBr2} < 0.7$. For $T_s > 35$ °C, this range extends further, such that a flux imbalance of $-1 < r_{MABr,SnBr2} < 1$ still results in a stoichiometric film. This result suggests that $MASnBr_3$ films grown using CGAVD have a self-correcting window in the sense that the surface adsorption and reaction probabilities of MABr and/or $SnBr_2$ adjust to balance their net incorporation rates into the film. This relaxes the need to balance the precursor fluxes exactly in order to deposit phase-pure $MASnX_3$ films.

Another important benefit of this "self-correcting" window is the ability to vary the film morphology while maintaining nominal film stoichiometry and phase purity, essentially decoupling morphological control from compositional control.

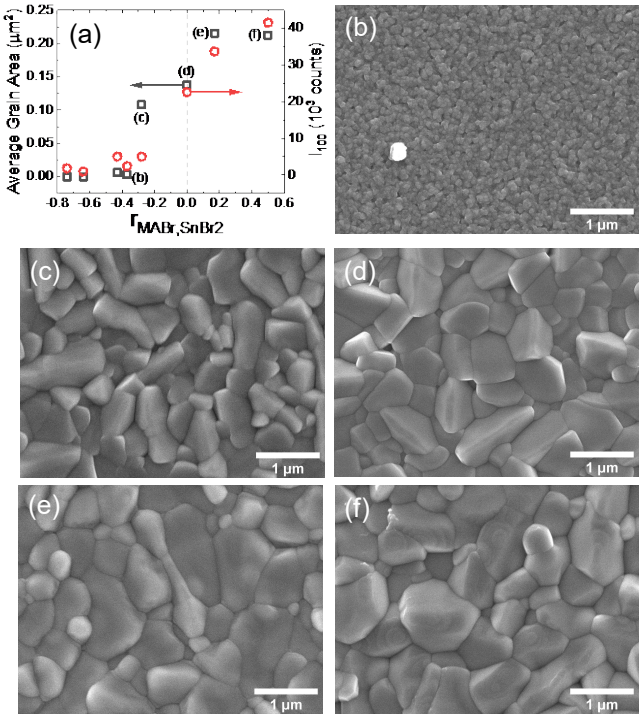

Fig. 4 Film grain size (black squares) and crystallinity (red circles) for $MASnBr_3$ on quartz within the stoichiometric region but at different MABr:$SnBr_2$ flux ratios. $r_{MABr,SnBr2}$ corresponding to each image in (b)-(f) is labelled in (a). Here, the flux ratio was controlled by changing T_{SnBr2}. All other variables remained constant for these depositions: $\dot{V}_{CG,\,SnBr2} = 6$ sccm, $\dot{V}_{CG,\,MABr} = 3$ sccm, $\dot{V}_{DIL} = 191$ sccm, $T_{MABr} = 136$ °C, $T_g = 300$ °C, $T_s = 30$ °C, and $P = 2.6$ Torr.

Fig. 4a shows average grain area and the intensity of the (100) peak (normalized by film thickness) as a function of $r_{MABr,SnBr2}$ for the stoichiometric films in Fig. 4b-f. XRD patterns are shown in Fig. S7. In this case, $r_{MABr,SnBr2}$ was tuned by adjusting the $SnBr_2$ source temperature while keeping all other experimental variables constant. The intensity of the (100) diffraction is a measure of the film crystallinity and Fig. 4 shows that it changes dramatically with changes in $r_{MABr,SnBr2}$, increasing by an order of magnitude from $r_{MABr,SnBr2} = 0.27$ to $r_{MABr,SnBr2} = 0.5$. Average grain size has a similar trend, increasing from 0.003 μm² to over 0.2 μm² for $-0.75 < r_{MABr,SnBr2} < 0.5$.

Morphological Control *via* P and T_s

For a given precursor flux ratio $r_{MABr,SnBr2}$, the morphology of metal halide perovskite films can be further tuned using parameters such as P, $\dot{V}_{DIL}$, and T_s. Fig. 5 shows the impact of deposition pressure P and substrate temperature T_s on grain size and orientation factor for phase-pure $MASnBr_3$ films with constant $r_{MABr,SnBr2} \cong 1$. Grain area distributions are shown in Fig. S8, and representative SEM images are shown in Fig. S9. The texture coefficient $TC_{h_i k_i l_i}$ is calculated using Eqn. 4:[81]

$$TC_{h_ik_il_i} = \frac{I_{h_ik_il_i}}{I_{0,h_ik_il_i}}\left[\frac{1}{N}\sum_1^N \frac{I_{h_ik_il_i}}{I_{0,h_ik_il_i}}\right]^{-1} \quad \text{Eqn. 4}$$

where $I_{h_ik_il_i}$ is the intensity of the measured $(h_ik_il_i)$ diffraction peak, $I_{0,h_ik_il_i}$ is the intensity of the calculated $h_ik_il_i$ for a powdered crystalline sample, and $N = 5$ is the number of peaks considered. For a polycrystalline sample $TC_{h_ik_il_i} = 1$, whereas $TC_{h_ik_il_i} < 1$ indicates supressed $(h_ik_il_i)$ peaks and $TC_{h_ik_il_i} > 1$ indicates orientation in the $(h_ik_il_i)$ direction.

Fig. 5a shows that increasing T_s results in larger grain sizes, with grain size increasing from $T_s = 30$ °C to $T_s = 70$ °C for all pressures. Interestingly, the degree to which deposition pressure impacts grain size appears to increase with increasing T_s. For $T_s = 30$ °C, changing the deposition pressure from 0.3 to 10 Torr has relatively little impact on average grain size. For $T_s = 50$ °C, however, the same change in pressure results in an approximate doubling of grain size. For $T_s = 70$ °C this effect is even more dramatic, as grain size triples from $P = 0.3$ Torr to $P = 10$ Torr. Grain size distributions (Fig. S8) have a similar dependence on P and T_s; at low substrate temperatures ($T_s = 30$ °C), deposition pressure has little impact on grain size distributions, but for $T_s > 30$ °C, the range of grain areas increases with both P and T_s.

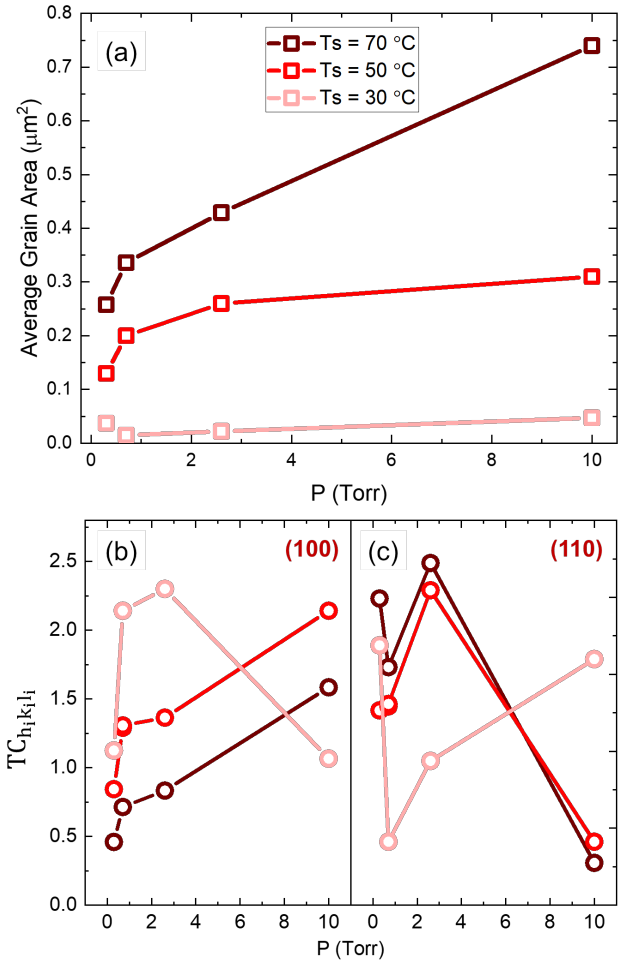

Fig. 5 Film grain size (a) and texture coefficient $TC_{h_ik_il_i}$ (b,c) as a function of P and T_s for $MASnBr_3$ on quartz. All other variables remained constant for these depositions: $\dot{V}_{CG,\,SnBr2} = 4$ sccm, $\dot{V}_{CG,\,MABr} = 3$ sccm, $\dot{V}_{DIL} = 20$ sccm (for $P < 2.6$ Torr) or $\dot{V}_{DIL} = 200$ sccm (for $P \geq 2.6$ Torr), $T_{SnBr2} = 233$ °C, $T_{MABr} = 142$ °C, and $T_g = 300$ °C. For all depositions, $r_{MABr,SnBr2} \cong 1$. Grain size distributions, representative SEM images, and texture coefficients for additional peaks are shown in Fig. S8 – S10.

Film texturing can also be tuned using P and T_s. Fig. 5b and 5c show the texture coefficient for (100) and (110) peaks calculated using Eqn. 4, demonstrating the ability to preferentially orient or supress these peaks. $TC_{h_ik_il_i}$ for additional peaks are shown in Fig. S10. As with grain size, the dependence of $TC_{h_ik_il_i}$ on P varies with substrate temperature. Whereas the orientation of the (100) peak increases monotonically with increasing pressure for $T_s \geq 50$ °C, this trend is not monotonic for $T_s = 30$ °C. For the $T_s \geq 50$ °C, the (110) peak can be nearly completely supressed at $P = 10$ Torr, but it is slightly oriented for $T_s = 30$ °C and $P = 10$ Torr.

Fig 6. shows calculated and measured deposition rates for the films in Figs. 5 and S8. Interestingly, deposition rates calculated including total precursor fluxes (Eqn. S27) greatly overestimate the measured values, whereas excluding excess precursor flux (Eqn. S26) results in a calculated deposition rate that agrees well with experiment. This good agreement is further evidence of the stoichiometrically self-correcting behavior of $MASnBr_3$ deposited using CGAVD. Furthermore, Fig. 6 shows that

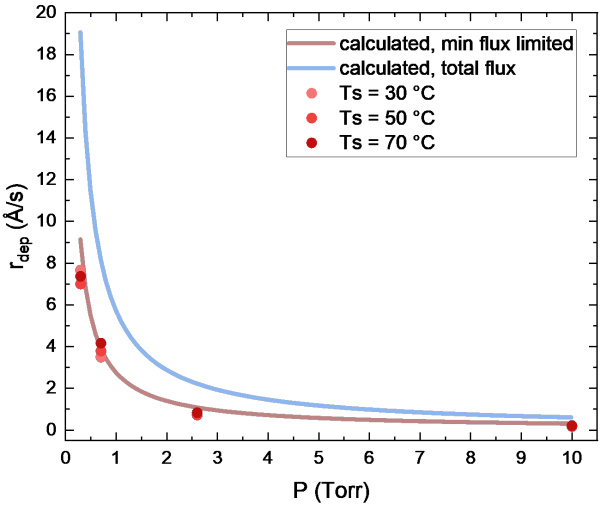

Fig. 6 Measured and calculated deposition rates corresponding to the films in Figs. 5 and S8 – S10. Measured deposition rates agree well with calculated values when excess precursor flux is excluded (Eqn. S26). Calculated deposition rates that include total flux of both precursors (Eqn. S27) significantly overestimates deposition rate – indicating that excess precursor flux is rejected during $MASnBr_3$ film formation using CGAVD.

substrate temperatures used here have a minimal effect on deposition rate, allowing the independent tuning of morphology with T_s and P.

Electrical Properties vs. Stoichiometry

To probe the electrical properties of CGAVD-grown $MASnBr_3$ and $MASnI_3$ films, 4-terminal resistivity measurements were taken at 280 K. As reported elsewhere,[82,83] $MASnBr_3$ films were much more resistive than $MASnI_3$ films. Resistivities of 3 Ω cm and 7x10^4 Ω cm are obtained for $MASnI_3$ and $MASnBr_3$, respectively, consistent with previous reports.[82–84]

For $MASnI_3$, the lower resistivity enabled Hall effect measurements to be made as a function of excess precursor species (I_{MAI}/I_{MASnI_3} or I_{SnI_2}/I_{MASnI_3}). Fig. S11 shows the corresponding resistivity (ρ), hole concentration, and Hall mobility for $MASnI_3$ films at 280 K. All $MASnI_3$ films were *p*-type, with hole concentration rising by nearly one order of magnitude from ~2×10^{19} cm^{-3} to ~10^{20} cm^{-3}, as the film composition moves from SnI_2 excess to MAI excess. *p*-type conduction is typically associated with the oxidation of Sn^{2+} to Sn^{4+},[84–86] and the relatively high hole concentrations (10^{19} – 10^{20} cm^{-3}) may be due to the lack of a reducing agent such as SnF_2, as well as air exposure of the source material and films during loading and unloading from the CGAVD chamber and preparation for electronic transport measurements. Consequently, mobilities calculated assuming the Drude model (i.e., $\rho = 1/ep\mu$ where e is the electric charge) are relatively low for these films, ranging from 0.2 to 1.5 cm^2/Vs, compared to typical Hall mobilities reported in the literature for $MASnI_3$ (1.6 – 2320 cm^2/Vs).[82,87]

The carrier concentrations and mobilities reported herein are not optimized, and represent a relatively narrow range of the experimental parameter space. Optimization of electrical and optical properties as a function of deposition conditions, reducing agents (such as SnF_2), and minimized air exposure are ongoing.

Conclusion

This work presents a detailed treatment of the transport regimes and operating conditions required to grow high-quality halide perovskite thin films *via* a carrier-gas assisted vapor deposition (CGAVD) technique. While this technique has been previously explored in the context of organic semiconductors, it has yet to be fully harnessed for optimizing perovskite thin film synthesis. By developing and applying an analytical model for the deposition rates of MABr, MAI, $SnBr_2$, and SnI_2, we are able to synthesize uniform $MASnBr_xI_{3-x}$ thin films on a variety of substrates. By varying source material temperature, carrier gas flow rate, dilution gas flow rate, substrate temperature, and chamber pressure, we realize changes in the degree of crystallinity, grain orientation, and average grain size (from ~ 0.001 to $> 0.7\ \mu m^2$) for $MASnBr_3$ thin films. Preliminary measurements show resistivities of 3 Ω cm for $MASnI_3$ and 7x10^4 Ω cm for $MASnBr_3$ at 280 K. We systematically probe resistivity, hole concentration, and mobility for $MASnI_3$ films as a function of precursor excess, and find relatively high carrier concentrations likely associated with the lack of reducing agent and potential air exposure. The ability of films grown using CGAVD to stoichiometrically self-correct by rejecting excess precursors, even with substantially unbalanced precursor flux rates, underscores the robustness of this technique.

Conflicts of interest

There are no conflicts to declare.

Acknowledgements

This research was funded by the National Science Foundation (NSF) through an iSuperseed grant to the University of Minnesota MRSEC (DMR-1420013) and a grant from the University of Minnesota Institute on the Environment. The authors also acknowledge support from anonymous donors to ESA, Ronald A. and Janet A. Christenson, the 3M Science and Technology Fellowship, and the UMII MnDRIVE Graduate Assistantship. The authors thank John Suddard-Bangsund for helpful discussions. Parts of this work were carried out in the Characterization Facility, University of Minnesota, which receives partial support from NSF through the MRSEC program.

References

1 N. G. Park, M. Grätzel, T. Miyasaka, K. Zhu and K. Emery, *Nat. Energy*, 2016, **1**, 16152.
2 L. K. Ono, N.-G. Park, K. Zhu, W. Huang and Y. Qi, *ACS Energy Lett.*, 2017, **2**, 1749–1751.
3 Y.-S. Jung, K. Hwang, Y.-J. Heo, J.-E. Kim, D. Lee, C.-H. Lee, H.-I. Joh, J.-S. Yeo and D.-Y. Kim, *Appl. Mater. Interfaces*, 2017, **9**, 27832–27838.
4 J.-P. Correa-Baena, M. Saliba, T. Buonassisi, M. Grätzel, A. Abate, W. Tress and A. Hagfeldt, *Science (80-.).*, 2017, **358**, 739–744.
5 G. E. Eperon, T. Leijtens, K. A. Bush, R. Prasanna, T. Green, J. T.-W. Wang, D. P. McMeekin, G. Volonakis, R. L. Milot, R. May, A. Palmstrom, D. J. Slotcavage, R. A. Belisle, J. B. Patel, E. S. Parrott, R. J. Sutton, W. Ma, F. Moghadam, B. Conings, A. Babayigit, H.-G. Boyen, S. Bent, F. Giustino, L. M. Herz, M. B. Johnston, M. D. McGehee and H. J. Snaith, *Science (80-.).*, 2016, **354**, 861–865.
6 H. J. Snaith, *Nat. Mater.*, 2018, **17**, 372–376.
7 M. A. Green, A. Ho-Baillie and H. J. Snaith, *Nat. Photonics*, 2014, **8**, 506–514.
8 J. H. Heo, D. S. Lee, D. H. Shin and S. H. Im, *J. Mater. Chem. A*, 2018, **7**, 888–900.
9 N. J. Jeon, H. Na, E. H. Jung, T. Y. Yang, Y. G. Lee, G. Kim, H. W. Shin, S. Il Seok, J. Lee and J. Seo, *Nat. Energy*, 2018, **3**, 682–689.
10 K. Lin, J. Xing, L. N. Quan, F. P. G. de Arquer, X. Gong, J. Lu, L. Xie, W. Zhao, D. Zhang, C. Yan, W. Li, X. Liu, Y. Lu, J.

Kirman, E. H. Sargent, Q. Xiong and Z. Wei, *Nature*, 2018, **562**, 245–248.
11 X. Li, D. Bi, C. Yi, J. D. Décoppet, J. Luo, S. M. Zakeeruddin, A. Hagfeldt and M. Grätzel, *Science (80-.).*, 2016, **353**, 58–62.
12 D. Y. Son, J. W. Lee, Y. J. Choi, I. H. Jang, S. Lee, P. J. Yoo, H. Shin, N. Ahn, M. Choi, D. Kim and N. G. Park, *Nat. Energy*, 2016, **1**, 1–8.
13 S. Rafizadeh, K. Wienands, P. S. C. Schulze, A. J. Bett, L. C. Andreani, M. Hermle, S. W. Glunz and J. C. Goldschmidt, *ACS Appl. Mater. Interfaces*, 2019, **11**, 722–729.
14 T. B. Song, Q. Chen, H. P. Zhou, C. Y. Jiang, H. H. Wang, Y. Yang, Y. S. Liu, J. B. You and Y. Yang, *J. Mater. Chem. A*, 2015, **3**, 9032–9050.
15 Q. Wang, Y. Shao, Q. Dong, Z. Xiao, Y. Yuan and J. Huang, *Energy Environ. Sci.*, 2014, **7**, 2359–2365.
16 W. S. Yang, B.-W. Park, E. H. Jung, N. J. Jeon, Y. C. Kim, D. U. Lee, S. S. Shin, J. Seo, E. K. Kim, J. H. Noh and S. Il Seok, *Science (80-.).*, 2017, **356**, 1376–1379.
17 F. Wang, S. Bai, W. Tress, A. Hagfeldt and F. Gao, *npj Flex. Electron.*, 2018, **2**, 22.
18 M. M. Tavakoli, M. Saliba, P. Yadav, P. Holzhey, A. Hagfeldt, S. M. Zakeeruddin and M. Grätzel, *Adv. Energy Mater.*, 2018, **9**, 1802646.
19 T. Du, C. H. Burgess, C. T. Lin, F. Eisner, J. Kim, S. Xu, H. Kang, J. R. Durrant and M. A. McLachlan, *Adv. Funct. Mater.*, 2018, **28**, 1803943.
20 Y. Zhou, O. S. Game, S. Pang and N. P. Padture, *J. Phys. Chem. Lett.*, 2015, **6**, 4827–4839.
21 J.-P. Correa-Baena, W. Tress, K. Domanski, E. H. Anaraki, S.-H. Turren-Cruz, B. Roose, P. P. Boix, M. Grätzel, M. Saliba, A. Abate and A. Hagfeldt, *Energy Environ. Sci.*, 2017, **10**, 1207–1212.
22 J. J. Li, J. Y. Ma, Q. Q. Ge, J. S. Hu, D. Wang and L. J. Wan, *ACS Appl. Mater. Interfaces*, 2015, **7**, 28518–28523.
23 D. R. Tobergte and S. Curtis, *J. Chem. Inf. Model.*, 2013, **53**, 1689–1699.
24 T. S. Sherkar, C. Momblona, L. Gil-Escrig, J. Ávila, M. Sessolo, H. J. Bolink and L. J. A. Koster, *ACS Energy Lett.*, 2017, **2**, 1214–1222.
25 C. Gao, J. Liu, C. Liao, Y. Q. Ye, Y. Zhang, X. He, X. Guo, J. Mei and L. W. M. Lau, *RSC Adv.*, 2015, **5**, 26175–26180.
26 T.-W. Ng, C. Y. Chan, M.-F. Lo, Z. GUAN and C. Lee, *J. Mater. Chem. A*, 2015, **3**, Advance.
27 B. S. Kim, T. M. Kim, M. S. Choi, H. S. Shim and J. J. Kim, *Org. Electron. physics, Mater. Appl.*, 2015, **17**, 102–106.
28 L. E. Polander, P. Pahner, M. Schwarze, M. Saalfrank, C. Koerner and K. Leo, *APL Mater.*, 2014, **2**, 081503.
29 A. S. Subbiah, A. Halder, S. Ghosh, N. Mahuli, G. Hodes and S. K. Sarkar, *J. Phys. Chem. Lett.*, 2014, **5**, 1748–1753.
30 Q. Lin, A. Armin, R. Chandra, R. Nagiri, P. L. Burn and P. Meredith, *Nat. Photonics*, 2014, **9**, 106–112.
31 O. Malinkiewicz, C. Roldan-Carmona, A. Soriano, E. Bandiello, L. Camacho, M. K. Nazeeruddin and H. J. Bolink, *Adv. Energy Mater.*, 2014, **4**, 1400345.
32 M. Liu, M. B. Johnston and H. J. Snaith, *Nature*, 2013, **501**, 395–398.
33 J. Ávila, C. Momblona, P. P. Boix, M. Sessolo and H. J. Bolink, *Joule*, 2017, **1**, 431–442.
34 M. M. Tavakoli, L. Gu, Y. Gao, C. Reckmeier and J. He, *Nat. Sci. Reports*, 2015, **5**, 14083.
35 Y. Jiang, M. R. Leyden, L. Qiu, S. Wang, L. K. Ono, Z. Wu, E. J. Juarez-Perez and Y. Qi, *Adv. Funct. Mater.*, 2018, **28**, 1703835.
36 B. Wang and T. Chen, *Adv. Sci.*, 2016, **3**, 1500262.
37 P. Luo, Z. Liu, W. Xia, C. Yuan, J. Cheng and Y. Lu, *Appl. Mater. Interfaces*, 2015, **7**, 2708–2714.
38 M. R. Leyden, M. V Lee, S. R. Raga and Y. Qi, *J. Mater. Chem. A*, 2015, **3**, 16097–16103.
39 M. Tai, X. Zhao, H. Wei, G. Wang, F. Hao, X. Li, X. Yin, Y. Zhou, J. Han, Y. Wei, K. Jiang and H. Lin, *ACS Appl. Mater. Interfaces*, 2018, **10**, 26206–26212.
40 X. Zhu, D. Yang, R. Yang, B. Yang, Z. Yang, X. Ren, J. Zhang, J. Niu, J. Feng and S. F. Liu, *Nanoscale*, 2017, **9**, 12316–12323.
41 O. Malinkiewicz, A. Yella, Y. H. Lee, G. M. M. Espallargas, M. Graetzel, M. K. Nazeeruddin and H. J. Bolink, *Nat. Photonics*, 2013, **8**, 128–132.
42 C. Momblona, O. Malinkiewicz, C. Roldan-Carmona, A. Soriano, L. Gil-Escrig, E. Bandiello, M. Scheepers, E. Edri and H. J. Bolink, *APL Mater.*, 2014, **2**, 081504.
43 L. K. Ono, S. Wang, Y. Kato, S. R. Raga and Y. Qi, *Energy Environ. Sci.*, 2014, **7**, 3989–3993.
44 S. Wang, L. K. Ono, M. R. Leyden, Y. Kato, S. R. Raga, M. V Lee and Y. Qi, *J. Mater. Chem. A*, 2015, **3**, 14631–14641.
45 J. Teuscher, A. Ulianov, O. Müntener, M. Grätzel and N. Tétreault, *ChemSusChem*, 2015, **8**, 3847–3852.
46 D. Zhao, W. Ke, C. R. Grice, A. J. Cimaroli, X. Tan, M. Yang, R. W. Collins, H. Zhang, K. Zhu and Y. Yan, *Nano Energy*, 2016, **19**, 88–97.
47 C. Chen, H. Kang, S. Hsiao, P. Yang, K. Chiang and H. Lin, *Adv. Mater.*, 2014, **26**, 6647–6652.
48 H. Hu, D. Wang, Y. Zhou, J. Zhang, S. Lv, S. Pang, X. Chen, Z. Liu, N. P. Padture and G. Cui, *RSC Adv.*, 2014, **4**, 28964–28967.
49 A. Ng, Z. Ren, Q. Shen, S. H. Cheung, H. C. Gokkaya, G. Bai, J. Wang, L. Yang, S. K. So, A. B. Djurišić, W. W. Leung, J. Hao, W. K. Chan and C. Surya, *J. Mater. Chem. A*, 2015, **3**, 9223–9231.
50 H. A. Abbas, R. Kottokkaran, B. Ganapathy, M. Samiee, L. Zhang, A. Kitahara, M. Noack and V. L. Dalal, *APL Mater.*, 2015, **3**, 016105.
51 D. Yang, Z. Yang, W. Qin, Y. Zhang, S. (Frank) Liu and C. Li, *J. Mater. Chem. A*, 2015, **3**, 9401–9405.
52 M.-C. Jung, S. R. Raga and Y. Qi, *RSC Adv.*, 2016, **6**, 2819–2825.
53 L. Gil-Escrig, C. Momblona, D. Forgács, S. Pla, F. Fernández-Lázaro, M. Sessolo, Á. Sastre-Santos and H. J. Bolink, *Org. Electron.*, 2016, **37**, 396–401.
54 A. A. Paraecattil, J. De Jonghe-Risse, V. Pranculis, J. Teuscher and J.-E. Moser, *J. Phys. Chem. C*, 2016, **120**, 19595–19602.
55 B. Saparov, J. P. Sun, W. Meng, Z. Xiao, H. S. Duan, O. Gunawan, D. Shin, I. G. Hill, Y. Yan and D. B. Mitzi, *Chem.*

Mater., 2016, **28**, 2315–2322.
56 K. Shum, Z. Chen, J. Qureshi, C. Yu, J. J. Wang, W. Pfenninger, N. Vockic, J. Midgley and J. T. Kenney, *Appl. Phys. Lett.*, 2010, **96**, 1–4.
57 X. Qiu, B. Cao, S. Yuan, X. Chen, Z. Qiu, Y. Jiang, Q. Ye, H. Wang, H. Zeng, J. Liu and M. G. Kanatzidis, *Sol. Energy Mater. Sol. Cells*, 2017, **159**, 227–234.
58 D. Moghe, L. Wang, C. J. Traverse, A. Redoute, M. Sponseller, P. R. Brown, V. Bulovic and R. R. Lunt, *Nano Energy*, 2016, **28**, 469–474.
59 M. R. Leyden, L. K. Ono, S. R. Raga, Y. Kato, S. Wang and Y. Qi, *J. Mater. Chem. A*, 2014, **2**, 18742–18745.
60 P. Luo, Z. Liu, W. Xia, C. Yuan and Y. Lu, *J. Mater. Chem. A*, 2015, **3**, 12443–12451.
61 P. Luo, Z. Liu, W. Xia, C. Yuan, J. Cheng, C. Xu and Y. Lu, *J. Mater. Chem. A*, 2015, **3**, 22949–22959.
62 Y. Peng, G. Jing and T. Cui, *J. Mater. Chem. A Mater. energy Sustain.*, 2015, **3**, 12436–12442.
63 Y. Peng, G. Jing and T. Cui, *RSC Adv.*, 2015, **5**, 95847–95853.
64 P. Fan, D. Gu, G.-X. Liang, J.-T. Luo, J.-L. Chen, Z.-H. Zheng and D.-P. Zhang, *Sci. Rep.*, 2016, **6**, 29910.
65 C. Momblona, L. Gil-Escrig, E. Bandiello, E. M. Hutter, M. Sessolo, K. Lederer, J. Blochwitz-Nimoth and H. J. Bolink, *Energy Environ. Sci.*, 2016, **9**, 3456–3463.
66 K. R. Catchpole, N. S. Lewis, G. G. Andersson, T. P. White, N. Wu, J. Peng, C. Samundsett, Y. Yin, Y. Wu, T. Duong, P. Phang, D. Yan, Y. Wan, S. Yalamanchili, D. A. Jacobs, S. T. Omelchenko and H. Shen, *Sci. Adv.*, , DOI:10.1126/sciadv.aau9711.
67 L. Meng, J. You, T. F. Guo and Y. Yang, *Acc. Chem. Res.*, 2016, **49**, 155–165.
68 L. K. Ono, M. R. Leyden, S. Wang and Y. Qi, *J. Mater. Chem. A*, 2016, **4**, 6693–6713.
69 K. Vasseur, C. Rolin, S. Vandezande, K. Temst, L. Froyen and P. Heremans, *J. Phys. Chem. C*, 2010, **114**, 2730–2737.
70 F. Yang, M. Shtein and S. R. Forrest, *J. Appl. Phys.*, , DOI:10.1063/1.1941480.
71 M. Shtein, H. F. Gossenberger, J. B. Benziger and S. R. Forrest, *J. Appl. Phys.*, 2001, **89**, 1470–1476.
72 F. Yang, M. Shtein and S. R. Forrest, *Nat. Mater.*, 2005, **4**, 37–41.
73 M. Shtein, J. Mapel, J. B. Benziger and S. R. Forrest, *Appl. Phys. Lett.*, 2002, **81**, 268–270.
74 M. Baldo, M. Deutsch, P. Burrows, H. Gossenberger, M. Gerstenberg, V. Ban and S. Forrest, *Adv. Mater.*, 1998, **10**, 1505–1514.
75 M. R. Leyden, L. Meng, Y. Jiang, L. K. Ono, L. Qiu, E. J. Juarez-Perez, C. Qin, C. Adachi and Y. Qi, *J. Phys. Chem. Lett.*, 2017, **8**, 3193–3198.
76 M. R. Leyden, Y. Jiang and Y. Qi, *J. Mater. Chem. A*, 2016, **4**, 13125–13132.
77 P. S. Shen, J. S. Chen, Y. H. Chiang, M. H. Li, T. F. Guo and P. Chen, *Adv. Mater. Interfaces*, 2016, **3**, 1–8.
78 Y. Wang, X. Sun, Z. Chen, Y. Sun, S. Zhang and T. Lu, 2017, **1702643**, 1–8.
79 F. Hao, C. C. Stoumpos, D. H. Cao, R. P. H. Chang and M. G. Kanatzidis, *Nat. Photonics*, 2014, **8**, 489–494.
80 M. L. Lai, T. Y. S. Tay, A. Sadhanala, S. E. Dutton, G. Li, R. H. Friend and Z. K. Tan, *Phys. Chem. Lett.*, 2016, **7**, 2653−2658.
81 Y. Wang, W. Tang and L. Zhang, *J. Mater. Sci. Technol.*, 2015, **31**, 175–181.
82 M. Konstantakou and T. Stergiopoulos, *J. Mater. Chem. A*, , DOI:10.1039/c7ta00929a.
83 H. Hasegawa and T. Inabe, 2016, 7043–7047.
84 C. C. Stoumpos, C. D. Malliakas and M. G. Kanatzidis, *Inorg. Chem.*, 2013, **52**, 9019–9038.
85 P. Xu, S. Chen, H.-J. Xiang, X.-G. Gong and S.-H. Wei, *Chem. Mater.*, 2014, **26**, 6068–6072.
86 J. S. Manser, A. Christians and P. V Kamat, , DOI:10.1021/acs.chemrev.6b00136.
87 L. M. Herz, , DOI:10.1021/acsenergylett.7b00276.
88 A. Dualeh, P. Gao, S. Il Seok, M. K. Nazeeruddin and M. Graetzel, *Chem. Mater.*, 2014, **26**, 6160–6164.
89 H. Gamsjager, T. Gajda, S. K. Saxena, J. Sangster and W. Voigt, *Chemical Thermodynamics of Tin - Volume 12*, OECD, 2012.
90 L. V. Gurvich, I. V. Veyts and C. B. Alcock, Eds., *Thermodynamic Properties Of Individual Substances: Elements And compounds*, CRC Press, 1st edn., 1990.

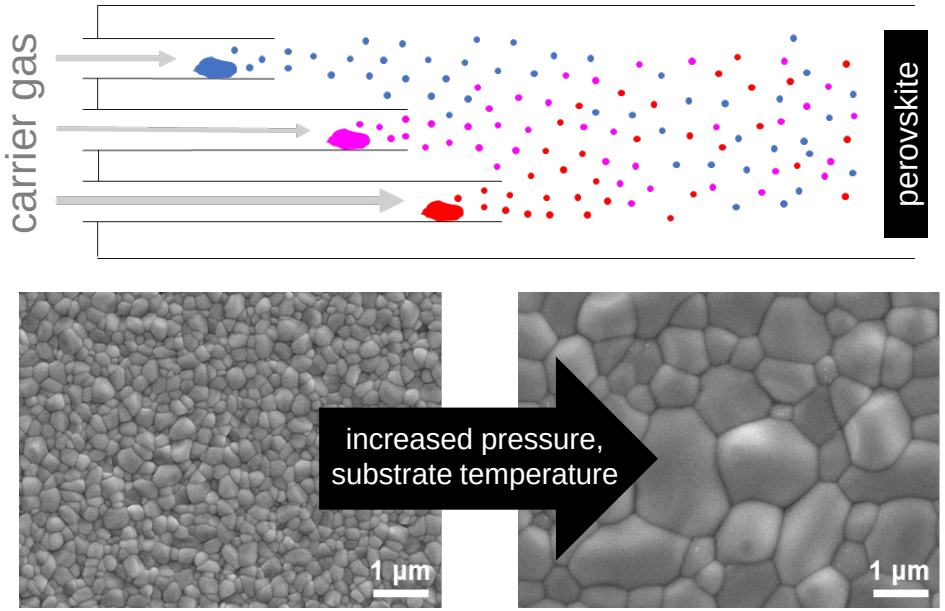

Detailed analysis of material transport in CGAVD enables highly tunable morphology and robust growth of metal halide perovskite thin films.